Matter

CellPress
OPEN ACCESS

Article

Effects of local compositional heterogeneity in mixed halide perovskites on blue electroluminescence

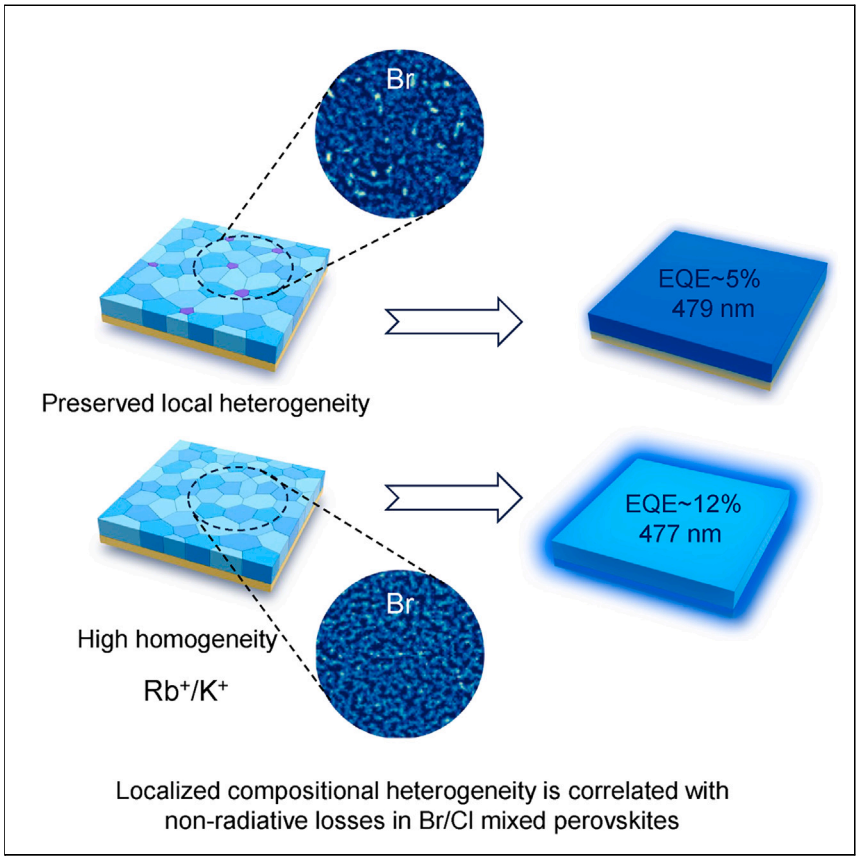

Until now, one of the major challenges preventing real-world applications has been the poor performance of blue emitters for perovskite light-emitting diodes. We find that even in the most advanced mixed halide blue emitters, localized heterogeneity exists, which works as a crucial yet overlooked factor that limits the performance of mixed halide blue perovskite emitters. We reveal the origination of heterogeneity by *in situ* measurements and propose a "cation alloying" strategy to mitigate the local heterogeneity.

Understanding
Dependency and conditional studies on material behavior

Xiyu Luo, Weidong Xu, Guanhaojie Zheng, ..., Jesper Wallentin, Wei Huang, Feng Gao

ifewdxu@nwpu.edu.cn (W.X.)
duanl@mail.tsinghua.edu.cn (L.D.)
iamwhuang@nwpu.edu.cn (W.H.)
feng.gao@liu.se (F.G.)

Highlights

The relation between defect and heterogeneity in mixed Br/Cl emitters is revealed

Observation of landscape for heterogeneity ranging from micro- to sub-micro regions

A "cation alloying" strategy is proposed to mitigate the local heterogeneity

Luo et al., Matter 7, 1054–1070
March 6, 2024
https://doi.org/10.1016/j.matt.2023.12.019

CellPress
OPEN ACCESS

Matter

Article

Effects of local compositional heterogeneity in mixed halide perovskites on blue electroluminescence

Xiyu Luo,[1,2] Weidong Xu,[2,3,*] Guanhaojie Zheng,[4] Sandhya Tammireddy,[5] Qi Wei,[6] Max Karlsson,[2] Zhaojun Zhang,[7] Kangyu Ji,[8,9] Simon Kahmann,[8,9] Chunyang Yin,[2] Yatao Zou,[2] Zeyu Zhang,[10] Huaiyu Chen,[7] Lucas A.B. Marçal,[7,11] Haifeng Zhao,[2] Dongxin Ma,[1] Dongdong Zhang,[1] Yue Lu,[10] Mingjie Li,[6] Carsten Deibel,[5] Samuel D. Stranks,[8,9] Lian Duan,[1,*] Jesper Wallentin,[7] Wei Huang,[3,*] and Feng Gao[2,12,*]

SUMMARY

Compositional heterogeneity is commonly observed in mixed bromide/iodide perovskite photoabsorbers, typically with minimal effects on charge carrier recombination and photovoltaic performance. Consistently, it has so far received very limited attention in bromide/chloride-mixed perovskites, which hold particular significance for blue light-emitting diodes. Here, we uncover that even a minor degree of localized halide heterogeneity leads to severe non-radiative losses in mixed bromide/chloride blue perovskite emitters, presenting a stark contrast to general observations in photovoltaics. We not only provide a visualization of the heterogeneity landscape spanning from micro-to sub-microscale but also identify that this issue mainly arises from the initially formed chloride-rich clusters during perovskite nucleation. Our work sheds light on a long-term neglected factor impeding the advancement of blue light-emitting diodes using mixed halide perovskites and provides a practical strategy to mitigate this issue.

INTRODUCTION

Compositional heterogeneity is a prevalent characteristic in state-of-the-art metal halide perovskites, mostly arising from the combined use of various cations and anions. Unlike conventional semiconductors such as silicon and gallium arsenide, perovskites have demonstrated exceptional tolerance to heterogeneity.[1–5] This unique property is evident from the excellent photovoltaic performance and high photovoltage in mixed halide/cation perovskite photoabsorbers, despite the fact that distinct chemical and structural heterogeneities spanning from nano- to micrometer scale are clearly visible. Detailed investigations suggest that the observed heterogeneity in perovskite photoabsorbers is not necessarily correlated with carrier mobilities and charge trapping.[6] In fact, recent studies pointed out that it could even be benign.[7,8] In brief, the nanoscale compositional gradients present in perovskite photoabsorbers facilitate carrier recombination away from defect-concentrated clusters through carrier funneling processes, thus making charge recombination more radiative.[4]

Although the impacts of compositional heterogeneity have been extensively studied in those low-bandgap perovskites for photovoltaic applications, there has been

PROGRESS AND POTENTIAL

Tuning the bromide/chloride ratio is one of the most popular strategies for producing ideal blue/deep blue electroluminescence. However, it is widely noted that photoluminescence quenching becomes severe with increasing chloride content in mixed halide blue perovskite emitters, featuring as the most critical issue impeding the breakthrough of blue perovskite light-emitting diodes (PeLEDs). This problem is generally attributed to the intrinsic defect intolerance of chloride perovskites, despite the fact that PLQY values approaching unity have been demonstrated in $CsPbCl_3$ nanocrystals. This paradox indicates that there are likely additional factors limiting the performance of mixed halide blue PeLEDs. Here, we prove a crucial yet overlooked factor localized compositional heterogeneity that limits the performance of mixed halide blue perovskite emitters. Also, we propose a practical approach to mitigate this issue. Our findings provide a guideline for the development of blue PeLEDs.

limited attention given to wide-bandgap chloride/bromide mixed perovskites. The latter is particularly important for developing blue perovskite light-emitting diodes (PeLEDs). Notably, the primary blue specified by Rec. 2020 standards requires Commission Internationale de l'Eclairage (CIE) coordinates of (0.131, 0.046), corresponding to a mixed halide perovskite with nearly equal amounts of bromide and chloride ions (e.g., $CsPbBr_{1.5}Cl_{1.5}$).[9–11] Such stoichiometry suggests potentially more severe heterogeneity compared with that in commonly used perovskite photoabsorbers (with bromide fractions typically less than ~17%).[12–14] Additionally, it is worth noting that compositional heterogeneity is associated with defect generation in conventional semiconductors, while chloride-mixed perovskites are much less tolerant to ionic defects compared with bromide/iodide ones.[15–18] As such, the influence of the chemical heterogeneity on charge carrier recombination in mixed chloride/bromide perovskites may differ significantly from that in perovskite photoabsorbers, and thus a deep and thorough understanding is highly required.

Here, we demonstrate that even a slight degree of compositional heterogeneity is crucial enough for triggering severe non-radiative losses in mixed bromide/chloride perovskites, featuring as one of the most critical issues hindering the development of blue PeLEDs. We also find that homogenizing the perovskite nucleation and subsequent grain growth can significantly mitigate defect generation associated with local heterogeneous halide distribution, resulting in improved quantum efficiencies of blue emitters and related devices. Overall, our work offers valuable insights into the rational engineering for high-efficiency blue PeLEDs with mixed halide strategy.

RESULTS

We select two representative mixed halide blue perovskite emitters to investigate the impact of local heterogeneity on radiative recombination, with a precursor stoichiometry of Cs^+:$(FA_{0.3-x}/Rb_x)^+$:Pb^{2+}:$[Br_{0.6}/Cl_{0.4}]^-$ = 1.2:0.3:1:3.5, where x = 0.1 or 0. Unless otherwise stated, a chelating additive, 3,6,9,12,15-pentaoxaheptadecane-1,17-bis-amine (NH_2-PEG_5-NH_2), is used to passivate the defects and retard the perovskite crystallization, which thus contributes to improved thin-film quality (Figure S1).[19,20] We added excess CsBr for all precursor solutions to eliminate the non-perovskite phase and reduce vacancy defects further.[10,21] The reasons for choosing these two perovskites are because (1) they are of high chloride contents, similar chemical stoichiometry, crystal structure, grain size, and morphology (Figure S2), and (2) we observe signs of the different chemical heterogeneity, that is, one shows completely symmetrical photoluminescence (PL) spectrum but a tiny high-energy emission shoulder is visible in another case evident in the logarithmic coordinates (Figure 1A). We refer the former (i.e., x = 0.1) and latter (i.e., x = 0) to target and control samples respectively. Such a weak high-energy component in control samples can hardly be observed in the linear coordinates (Figure S3) and the full width at half maximum (FWHM) of the emission linewidth remains unchanged (~16.0 nm), suggesting a very small degree of compositional heterogeneity despite high chloride content. Notably, a previously developed vapor-assisted crystallization technique is used in both cases to control the heterogeneity at an acceptable level which no longer affects the spectral stability of the resulting blue-emitting devices during operation.[12] We provide the details of samples with severe heterogeneity (without vapor treatment), including FWHM of emission, Urbach energy (E_U), and device characteristics in Figure S4, with detailed discussions summarized in Note S1.

As charge/energy transfer among the phases with different bandgap depends on the temperature, temperature-dependent PL measurement can resolve the hidden

[1]Key Lab of Organic Optoelectronics and Molecular Engineering of Ministry of Education, Department of Chemistry, Tsinghua University, Beijing 100084, China

[2]Department of Physics, Chemistry and Biology (IFM), Linköping University, Linköping, Sweden

[3]Frontiers Science Center for Flexible Electronics, Xi'an Institute of Flexible Electronics (IFE), Northwestern Polytechnical University, 127 West Youyi Road, Xi'an 710072, China

[4]Shanghai Synchrotron Radiation Facility (SSRF), Shanghai Advanced Research Institute, Chinese Academy of Sciences, Shanghai 201210, China

[5]Institut für Physik, Technische Universität Chemnitz, 09126 Chemnitz, Germany

[6]Department of Applied Physics, The Hong Kong Polytechnic University, Hung Hom, Kowloon, Hong Kong

[7]Synchrotron Radiation Research and NanoLund, Department of Physics, Lund University, 22100 Lund, Sweden

[8]Cavendish Laboratory, University of Cambridge, JJ Thomson Avenue, Cambridge CB3 0HE, UK

[9]Department of Chemical Engineering and Biotechnology, University of Cambridge, Philippa Fawcett Drive, Cambridge CB3 0AS, UK

[10]Institute of Microstructure and Property of Advanced Materials, Faculty of Materials and Manufacturing, Beijing University of Technology, Beijing 100124, China

[11]MAX IV Laboratory, Lund University, 22100 Lund, Sweden

[12]Lead contact

*Correspondence: ifewdxu@nwpu.edu.cn (W.X.), duanl@mail.tsinghua.edu.cn (L.D.), iamwhuang@nwpu.edu.cn (W.H.), feng.gao@liu.se (F.G.)

https://doi.org/10.1016/j.matt.2023.12.019

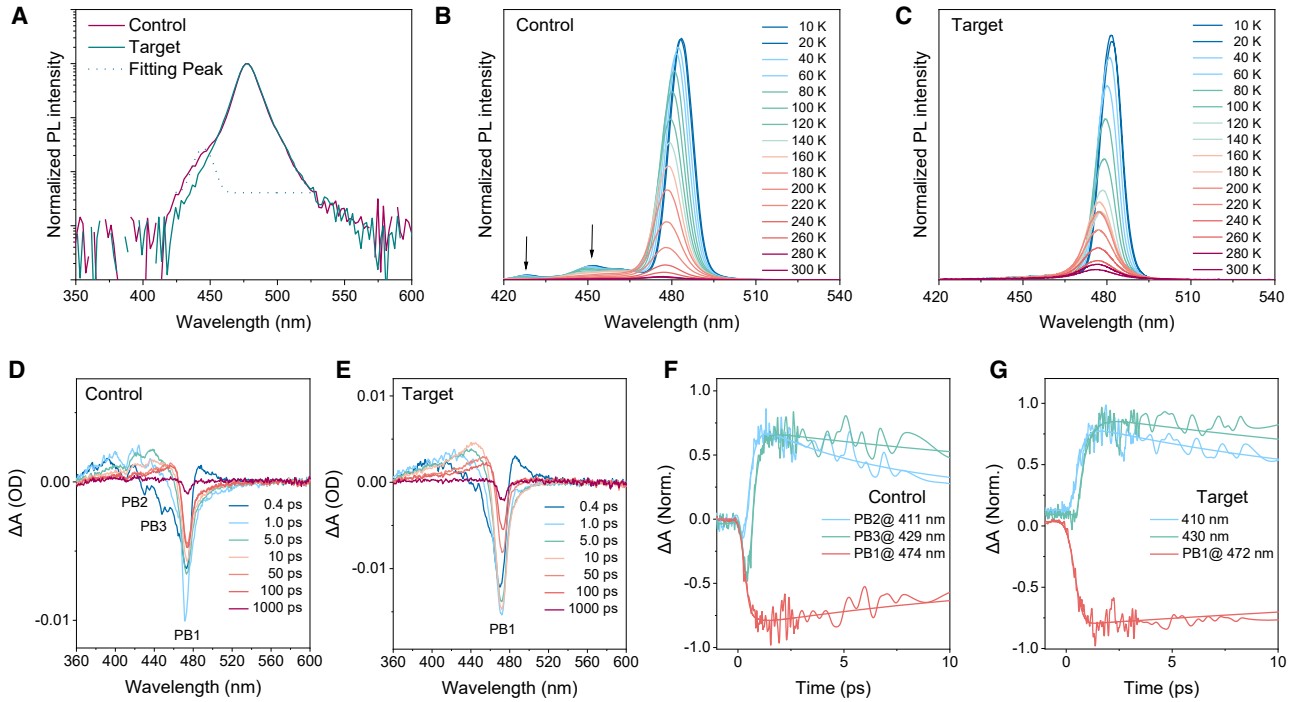

Figure 1. Heterogeneous optical properties

(A) Steady-state PL spectra in logarithmic coordinates.

(B and C) Temperature-dependent PL of control (B) and target samples (C).

(D and E) Transient absorption of control (D) and target films (E) with pump excitation at 350 nm. Here, three photobleaching bands are visible in the control samples (labeled as PB1, PB2, and PB3) but only one in the target sample (PB1).

(F and G) Comparison of temporal dynamics of photobleaching bands in control (F) and target samples (G).

emission features from high-energy species.[22] By following the evolution of PL spectra with decreasing temperatures (from 300 to 10 K), we observe the buildup of two high-energy emission bands peaking at ~428 and ~452 nm in the control samples (Figure 1B), suggesting the presence of high-energy species. In contrast, no additional PL peak is visible in the target samples (Figure 1C). In addition, we observe gradually narrowed emission linewidth, red-shifted emission peaks, and enhanced PL intensity in both cases with decreasing temperature (Figure 1; Figure S5), owing much to the reduced electron-phonon coupling and thermal activated non-radiative losses.[23]

To investigate the kinetics of exciton transfer between different phases, we conducted transient absorption (TA) measurements. We used a 350 nm ultraviolet femtosecond pulse laser as the pump source, which allowed us to generate strong signals from high-energy species (see more in Note S2 and Figure S6). For the control films, we observe a broad photobleaching signal with distinct high-energy shoulders emerging at early delay times (0.4 ps, labeled as PB2 and PB3). In addition, along with the increase of the delay time, the high-energy photobleaching PB2 and PB3 rapidly vanished, accompanied by the buildup of PB1 (Figure 1D). The fitting analysis of the time traces consistently yielded decay times of approximately ~0.27 ps for PB2 and ~0.25 ps for PB3, along with a rise time of ~0.28 ps for PB1 (Figure 1F). The well-matched decay and rise kinetics indicate fast exciton transfer from PB2 and PB3 to PB1. In comparison, we observe only slightly broadened photobleaching bands, with a slow rise time of ~0.45 ps, suggesting the absence of exciton transfer and thus a much better compositional heterogeneity in the target samples.

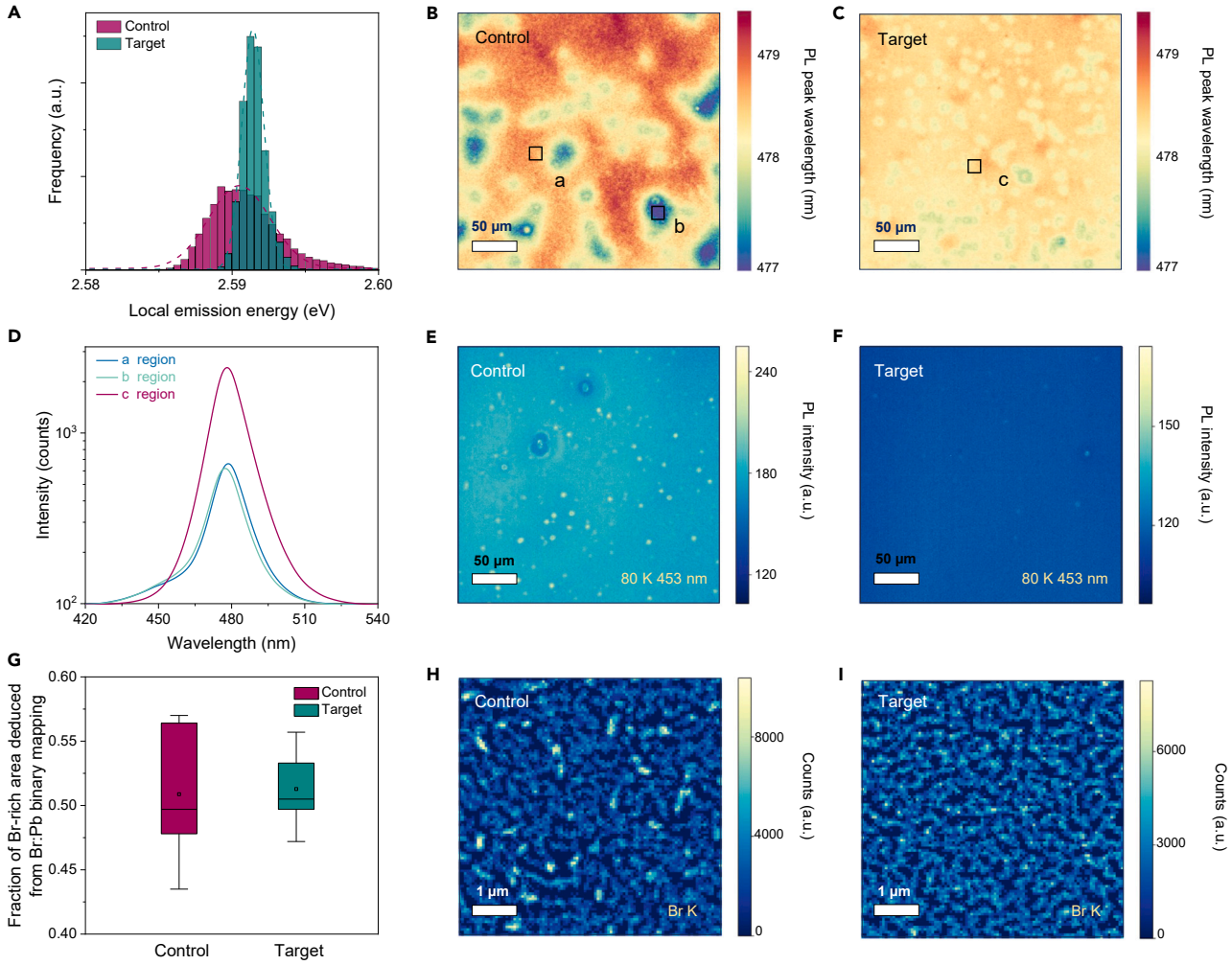

Figure 2. Landscape of local compositional distribution

(A) The histograms for photon energies of the emission peak extracted from (B) and (C). The dashed lines denote the normal fitting results.

(B and C) Hyperspectral microscopy of control (B) and target films (C). Scale bar: 50 μm.

(D) PL emission extracted from different regions (a, b, c) in (B) and (C).

(E and F) Hyperspectral PL intensity mapping for control (E) and target films (F) collected at 453 nm under cryogenic temperature (~80 K). Scale bar: 50 μm.

(G) The averaged area fraction of Br-rich area extracted from five different sub-regions of Br:Pb binary n-XRF maps (Figures S11 and S12).

(H and I) n-XRF maps of Br for control (H) and target samples (I). Scale bar: 1 μm.

To visually capture the local compositional heterogeneity, we use a wide-field, hyperspectral microscope to assess the spatially resolved luminescence properties at the microscale. We first measure the samples at room temperature (Figures 2A–2D). The histogram for the emission peak energies extracted from the hyperspectral images is shown in Figure 2A. Compared with the target samples, the control films display much more distinct discrepancies in emission peak wavelength across the entire mapping and hence a much wider distribution of energies. The shifts of the emission peak toward high photon energies can be as large as ~0.01 eV compared with the bin with the highest frequency. We further extract the PL spectra from two representative areas (20 × 20 μm) of the control film with contrasts in peak values, as well as an arbitrarily selected area for the target samples (Figure 2D). Compared with the control ones, the latter case displays symmetrical emission features even at microscale, confirming a homogeneous emission feature even at microscale.

To gather more information about the local scale of heterogeneity, we next conduct the hyperspectral microscope measurements at cryogenic temperature (~80 K), which excludes the impact from energy/charge transfer between different domains on optical properties in space. We show the PL intensity mapping images collected at 453 nm (Figures 2E and 2F), which is at the tail of the emission spectra. Compared with the target samples, much more bright emissive areas are visible in the control ones, further demonstrating the presence of localized heterogeneity. Importantly, we emphasize that even in the control samples, these heterogeneous emission features are relatively mild if compared with previously reported mixed halide perovskite photoabsorbers.[4] Furthermore, it is worth noting that the area exhibiting heterogeneous emission is extremely small. This suggests that the heterogeneity occurs in more localized regions that are beyond the resolution limit of our optical imaging technique.

With this in mind, we proceed to investigate the local fluctuation of the elements by synchrotron-based nano-X-ray fluorescence (n-XRF) measurements, aiming to gather more information about the length of heterogeneity at the sub-micro- or nanoscale as well as to reveal the origination of heterogeneity. The variation in elemental distribution is extracted by tracking the characteristic Cl L, Br K, Rb K, and Pb L lines in n-XRF (Figure S7). The size of each pixel is about 60 × 60 nm. As the signals of Cl and Rb are too weak to be accurately assessed, we mainly focus on the distribution of Br and Pb (Figures 2H and 2I; Figure S8). We show the Br maps as an example, from which the Br-concentrated aggregates with sizes ranging from ~200 to 300 nm clearly visible in control samples (Figure 2H). By contrast, the target samples give a higher uniformity of elemental distribution (Figure 2I). The discrepancies in localized elemental distribution between the samples are also visible in the intensity histogram extracted from the n-XRF maps (Figure S9). All these results confirm that the perovskites in target samples show higher uniformity of halide content across the entire film.

It is worth mentioning that the regions with higher Br contents in control films are often accompanied by a high amount of Pb, suggesting a potential impact of different perovskite thickness (Figure S8). To avoid this impact on our analysis, we resolve the fraction of Br-rich area with the binary (0 or 1) Pb: Br maps, which helped establish the correlation between chemical heterogeneity and high-energy optical components in the PL measurements. The binary maps are shown in Figure S10 and the detailed methods for the n-XRF analysis are summarized in Note S3. Our calculation yields a lower ratio of Br-rich area in control films (45.87%) with respect to target ones (49.53%). This, in turn, indicates the high contents of Cl-rich perovskites in the former. To assess the localized halide fluctuation further, we proceed to resolve the fraction of Br-rich/deficient areas of five sub-regions for each sample. Figure 2G displays the statistics of the normalized proportion of Br-rich areas from the corresponding binary maps. Accordingly, we find that statistically the control films are of a strong tendency to have Br-deficient area as suggested by the larger SD compared with the control case, further confirming the presence of Cl-rich clusters. The detailed results are summarized in Figures S11 and S12 and Table S1.

Having confirmed the differences in localized compositional homogeneity, we proceed to quantify their impact on the energetic heterogeneity by probing E_U. A low E_U value is commonly associated with a clean semiconductor.[24] Our fitting yields a much larger E_U value of ~84.8 meV compared with that of the target samples (~62.0 meV) (Figure S13). Although the latter is still strikingly higher in respect to pure phase perovskites which typically show an E_U value of 13.5–28.0 meV,[25,26]

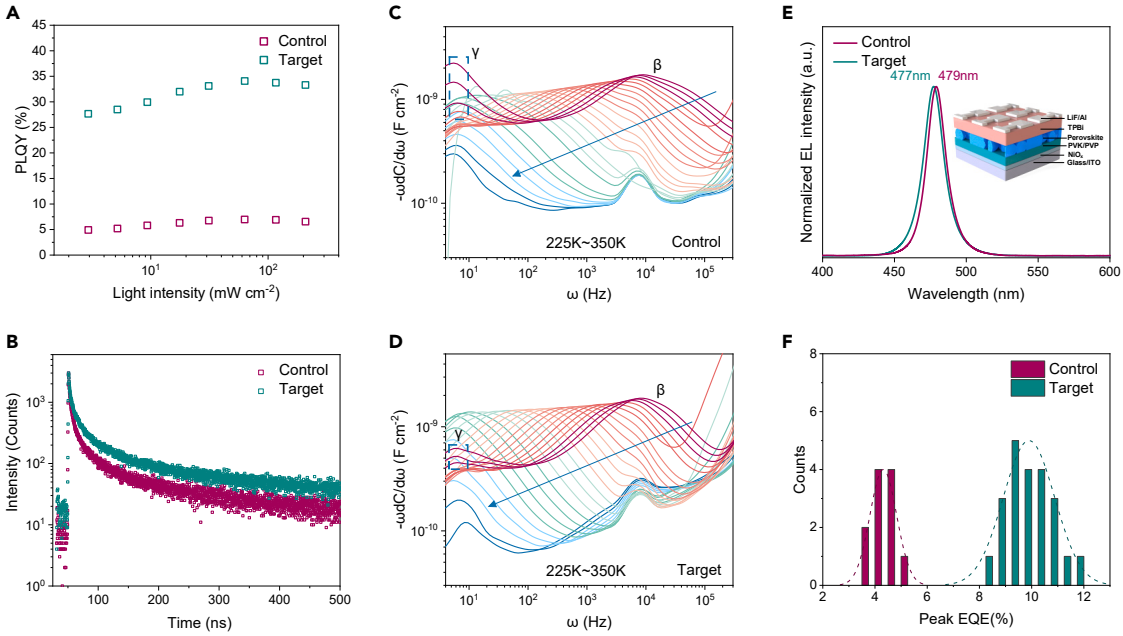

Figure 3. Impact of local compositional heterogeneity of halides on radiative recombination and trap states

(A) Fluence-dependent PLQYs.

(B) PL lifetime measured by TCSPC.

(C and D) Derivatives of temperature-dependent capacitance versus frequency plots for control (C) and target (D) devices. The blue arrows indicate temperature change from 350 to 225 K. The sets of capacitive responses are labeled as β and γ, respectively. The blue square highlights the vanished γ set of responses in the target samples.

(E) EL spectra and the device architecture (inset).

(F) Histograms of peak EQEs for the control and target devices.

the sharp contrast between our samples suggests a largely reduced electronic heterogeneity in the band edge as a consequence of improved local chemical homogeneity.

A clean sub-bandgap tail is usually linked to few defects and excellent PL properties.[24,26] We thus perform external PLQYs as a function of excitation fluence and time-resolved PL (TRPL) measurements to evaluate the impact of the compositional heterogeneity on radiative recombination. For both control and target samples, the PLQYs are increasing with enhancing excitation fluence, suggesting a competition between the first-order trap-assisted non-radiative recombination and bimolecular recombination in which the latter gradually becomes dominant. The target films present an overall enhancement of PLQYs across the entire range of excitation fluence, with a high peak PLQY of 34% compared with 7% of the other case (Figure 3A). In addition, the TRPL measurements demonstrate a prolonged PL lifetime of ~207 ns for the target samples compared with the control ones (~143 ns) (Figure 3B). Both indicate a mitigated charge trapping in the target samples with better homogeneity.

To further evaluate the defect generation and thus the quality of the samples, we measure thermal admittance spectroscopy (TAS), which is able to probe the dynamics of ionic and electronic defects. The capacitance-frequency plots and their derivations are shown in Figures S14 and 3C and 3D, respectively. Two sets of responses are clearly visible at high and low-frequency regions respectively. We refer the set of faster responses to β and the slower ones to γ. In light of the response

dynamics, as well as our previous studies on deep-level transient spectroscopy (DLTS) temperature-dependent conductivity, both β and γ responses can be assigned to mobile ionic defects.[27,28] We show the Arrhenius plots of β responses in Figure S15, from which we deduce the ion migration activation energy (E_A), ion diffusion coefficient (D_{avg}), and concentration of total ionic defects (N) (Table S2; see the theoretical derivation formula of TAS in Note S4).[29] The most striking difference happens to N, which roughly decreases to a quarter in target devices (6.60×10^{13} cm^{-3}) compared with that of control ones (2.44×10^{14} cm^{-3}). Accordingly, further analysis on thermodynamic properties yields an absolute formation entropy (S_f) value of ionic defect pairs of 23.0 eV K^{-1}, which is higher than that of control sample (21.7 eV K^{-1}). Such a difference implies more ordered perovskite crystal structures and fewer defects in target samples. More important, the γ signals for target devices are too weak to be assessed, suggesting that at least one class of ions becomes much less mobile. We thus conclude that ion migration is significantly inhibited in target samples, which is in turn a further sign of fewer point defects that usually work as ion hopping channels.[30] All these results imply that the films with better homogeneity are of fewer defects, analogous to silicon and III-V semiconductors.[4,31–34]

The reduced defect concentration achieved by high compositional homogeneity also gives rise to superior PeLED performance. Our device architecture is composed of indium tin oxide (ITO)/nickel oxide nanocrystals (NiO_x NC; ~10 nm)/poly(9-vinylcarbazole) (PVK): polyvinylpyridine (PVP; ~10 nm)/blue-emitting perovskites/2,2′,2″-(1,3,5-benzinetriyl)tris(1-phenyl-1*H*-benzimidazole) (TPBi; 45 nm)/lithium fluoride (LiF; ~1 nm)/aluminum (Al, ~100 nm) (Figure 3E, inset). The devices with target films yield a bright blue emission peaking at ~477 nm with a narrow FWHM of 16.0 nm and CIE coordinates of (0.105, 0.130) (Figure 3E; Figure S16), slightly blue-shifted compared with the control devices (479 nm, Figure 3E). The champion device for the target gives a peak external quantum efficiency (EQE) as high as 12.0% (Figure S17B). The peak EQE histogram for target devices shows an average EQE value of 9.9% with a low relative SD of 0.99%, in comparison with the control devices showing an average value of 4.3% with an SD of 0.51% (Figure 3F). The characteristics of representative control and target devices are summarized in Figures S17 and S18 and further discussed in Note S5.

Having unveiled the detrimental effects of local chemical fluctuation on perovskite film quality and device performance, the next question that arises is how to achieve a high homogeneity in mixed halide blue perovskite emitters. Considering the excellent performance of our target samples, a deep and thorough understanding of its crystallization process could give a general guidance toward rational material engineering. Apparently, the key component of our case includes a minimal amount of Rb ions as it is the only difference between these two samples. The first possibility is that the Rb ions could narrow the compositional distribution of mixed halide plumbates (e.g., $[PbX_3]^-$) in the solution, and thus homogenize the structures of perovskite during nucleation. Such an effect has been previously demonstrated by loading polymer additives into perovskite precursor solution.[10] We thus performed high-performance liquid chromatography electrospray ionization time-of-flight mass spectrometry (HPLC-ESI-TOF-MS) to characterize the constituents in the precursor solution with or without Rb^+. However, both indicate the co-existence of various halide plumbates, including $[PbCl_2Br]^-$, $[PbClBr_2]^-$, and $[PbBr_3]^-$ (Figure S19). Furthermore, no significant difference in intensity of the respective fragment ion is observed between the two samples. As such, we believe that Rb^+ addition has a very limited effect on the coordination environment of Pb^{2+} in the precursor solution.

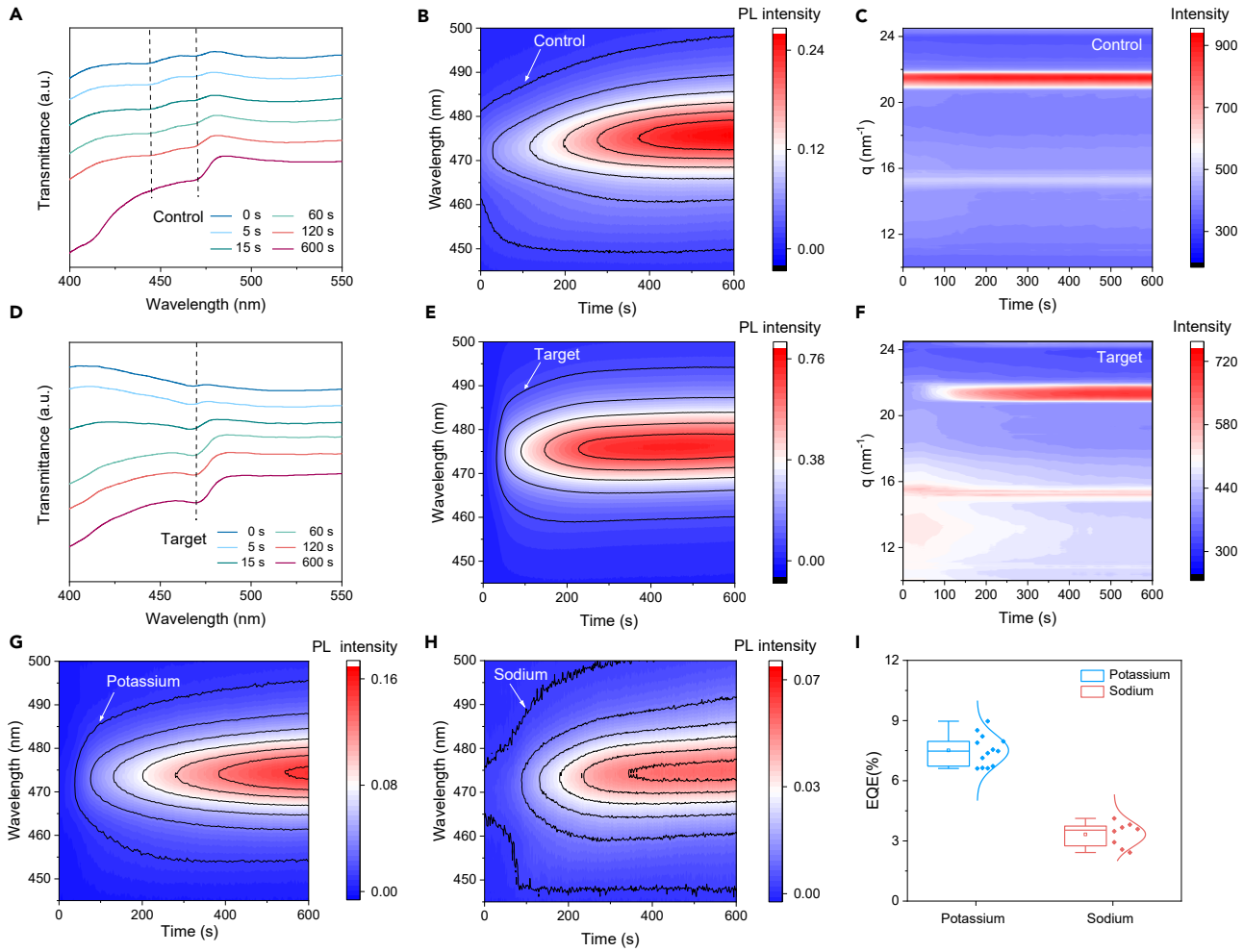

Figure 4. Monitoring the crystal growth of perovskite films

(A–F) Evolution of transmittance (A and D), PL spectra (B and E), and GIWAXS scattering intensity versus *q* (C and F) as a function of time for control (A–C) and target perovskite films (D–F) during vapor-assisted crystallization treatment. The dashed lines in (A) and (D) denote the excitonic features.

(G and H) PL evolution of K^+ (G) and Na^+ films (H).

(I) A summary of peak EQEs of devices prepared with K^+ or Na^+ addition; the boxes in Figure 4I denote a region containing 25%–75% of the data points; the lines and the squares within the boxes indicate the mean and median values, respectively; the top and bottom lines out of the boxes suggest the maximum and minimum values, respectively; the curves denote the Gaussian distribution.

Alternatively, it is possible for Rb^+ to affect the crystallization process during the stage of film formation. We use various *in situ* measurements to track the crystal growth during the vapor treatment, which is believed to be the most critical procedure for determining the film quality (as discussed in Note S1).[12] The samples without Rb^+ are investigated as well for comparison. We show the evolutions of transmittance and PL characteristics as a function of time in Figures 4 and S20. The most obvious difference appears in the initial stage (0 s) where the target films show only one excitonic feature close to the absorption onset along with a single and narrow PL emission (Figures 4D, 4E, and S20B). By contrast, an additional excitonic peak away from the onset is visible in transmittance spectra of control samples (Figure 4A), accompanied by a distinct PL shoulder that emerged at shorter wavelengths (Figure 4B; Figure S20A). These correspond well to the optical features of Cl-rich domains in control perovskite films. Following the evolution of time, the high-energy features are gradually diminished until hardly discernible, along with a slightly

reduced bandgap of the major component. These observations are consistent with our previous finding that a vapor-assisted Br/Cl exchange process governed by chemical equilibrium is occurring to homogenize the halide distribution.[12] We thus speculate that the chemical heterogeneity in the perovskites comes from the initially formed Cl-rich clusters during perovskite nucleation, which can hardly be healed entirely despite the vapor treatment and thermal annealing.

The formation of Cl-rich clusters is further confirmed by transmittance electron microscopy (TEM) measurements. We prepared the precursor samples by drop-casting the respective solution on copper grids without thermal annealing. We note that the perovskite nano-grains or clusters are readily found across the entire region in control samples. We show a representative TEM image in Figure S21A, from which the halide fluctuation can be visualized by resolving the lattice space of different crystals. Notably, most of the areas in target ones are covered by amorphous substances with few nanocrystals embedded, suggesting that perovskites are more difficult to form with Rb ions (Figure S21B).

We next perform *in situ* grazing-incidence wide-angle X-ray scattering (GIWAXS) measurements to further investigate the differences in crystallization process. The evolution of integrated scattering intensity as a function of time is shown in Figures 4C and 4F. For both cases, we observe gradual saturations of scattering intensity over time as a result of perovskite crystallization. The control films show two distinct scattering signals from the very beginning, with q values of ~15.3 and ~21.5 nm^{-1}, assigned to (110) and (200) planes of the perovskites, respectively. In comparison, these scattering peaks can hardly be well distinguished until 100 s of the treatment for target cases. These results are consistent with the TEM results, collectively indicative of a retarded perovskite crystallization with Rb^+ addition.

To generalize our findings, we proceed to investigate the impact of other alkali cations on grain growth and device performance, including potassium and sodium (K^+ and Na^+). Similarly, the K^+ and Na^+ addition do not alter the crystal structure as suggested by the X-ray diffraction (XRD) patterns (Figure S22). The results of *in situ* PL measurements are shown in Figures 4G and 4H and Figure S23. Notably, the addition of K^+ exhibits a similar effect to the Rb^+ case, where no distinct signs of Cl-rich clusters are observed throughout the entire crystallization process. Conversely, the addition of Na^+ has a limited impact on homogenizing the grain growth, as evident from the emergence of clear high-energy components in the PL spectra. Figure 4I shows a summary of peak EQEs of K^+ and Na^+ devices. The former offers a decent averaged EQE value of ~7.5%, much higher than that of the latter (~3.3%). The *J-V* characteristics of their champion devices are shown in Figure S24. The comparison of K^+ and Na^+ samples further confirm the detrimental effects of heterogeneous grain growth on device performance. In addition, we note that the performance of K^+-devices is slightly lower compared with those of Rb^+ devices (target). We speculate that Rb ions are of better ability in homogenizing the grain growth, as indicated by the narrower PL emission compared with that of K^+ samples during the initial stage of crystallization (Figures 4E and 4G).

DISCUSSION

Taking all the results mentioned hereinbefore, we can explain a complete picture of how local compositional heterogeneity affects mixed Br/Cl perovskites and the way to solve it. In conventional III-V semiconductors, non-intentional compositional heterogeneity is usually coupled with dislocations, which are also believed to be the

gathering centers for vacancy dominant point defects.[35–37] Similar chemical heterogeneity spanning from nano- to micrometer scale is also demonstrated in perovskites.[4,32,38] However, away from the consensus learned from conventional semiconductors, perovskites are believed to be tolerant to the chemical heterogeneity that has a limited effect on device performance. One excellent example is the golden recipe of alloying perovskites, i.e., $FA_{0.79}MA_{0.16}Cs_{0.05}Pb(I_{0.83}Br_{0.17})_3$, which are widely used for producing high-performance solar cells with minimal voltage losses despite distinct compositional heterogeneity.[4,34] These results differ from the current observations that the chemical heterogeneity is critical for non-radiative losses in mixed Br/Cl perovskites. One reasonable explanation is that the defects in Cl-rich perovskites are of a much stronger tendency to create deep-level traps with respect to Br/I counterparts because of their large bandgap, therefore eventually leading to a completely different effect of local heterogeneity.[4,15,16,38,39] In addition, considering that nano-crystals usually are of excellent compositional homogeneity, our findings also rationalize the general observations that the PLQY gap between mixed Br/Cl perovskite thin films and nano-crystals is much larger than that between those of Br/I anions.[12,40,41]

Our results also point out that the compositional heterogeneity mainly arises from the heterogeneous crystal growth that Cl-rich perovskite clusters crystalize ahead of those approaching chemical equilibrium. This is caused by the distinct discrepancies in the solubility of $CsPbX_3$ with different chloride contents. Such clusters are partially preserved in the resulted perovskites despite the following elemental homogenizing process during vapor-assisted crystallization. Instead, Rb^+ addition leads to an amorphous intermediate state, suppressing the origination of heterogeneity, i.e., chloride clusters, from the first place and thus leading to improved homogeneity of perovskites. We believe that this effect is achieved by formation of Cs/Rb cation alloy which alters the supersaturation of Cl-rich domains and/or enlarges the formation energy of perovskites. It thus leads to the changes in nucleation kinetics, as indicated by simultaneously retarded perovskite crystallization. With this in mind, one can expect that the Rb ions should be evenly distributed within the films instead of being Rb-rich clusters as reported previously.[42,43] Our energy-dispersive X-ray spectroscopy (EDX)/scanning transmission electron microscopy (STEM) and n-XRF tests consistently show no evidence of any Rb-concentrated clusters (Figures S8E and S25), despite the strong X-ray response signals of Rb. This speculation is further evident by the gradually decreased effects from Rb^+ to Na^+, as a larger mismatch in ionic radius with Cs^+ makes more difficulties in the formation of cation alloy and relevant alloy perovskites. However, we acknowledge that our target perovskites still exhibit some degree of local heterogeneity, as suggested by the large E_U (~62.0 meV). Therefore, additional material engineering toward more homogenized elemental distribution would be highly desired for achieving high-performance blue PeLEDs. The influences of crystallization process on local compositional homogeneity and relevant thin-film quality are depicted in Figure 5.

Conclusions

In conclusion, our study has revealed that local chemical heterogeneity in mixed bromide/chloride perovskites plays a detrimental role in causing substantial non-radiative losses. This critical issue mainly stems from the non-equilibrium perovskite crystallization that chloride-rich perovskite clusters form initially and are preserved during the whole process of grain growth. We have proposed and demonstrated that retarding perovskite crystallization is crucial for suppressing cluster formation and achieving improved homogeneity. Our results have highlighted that further

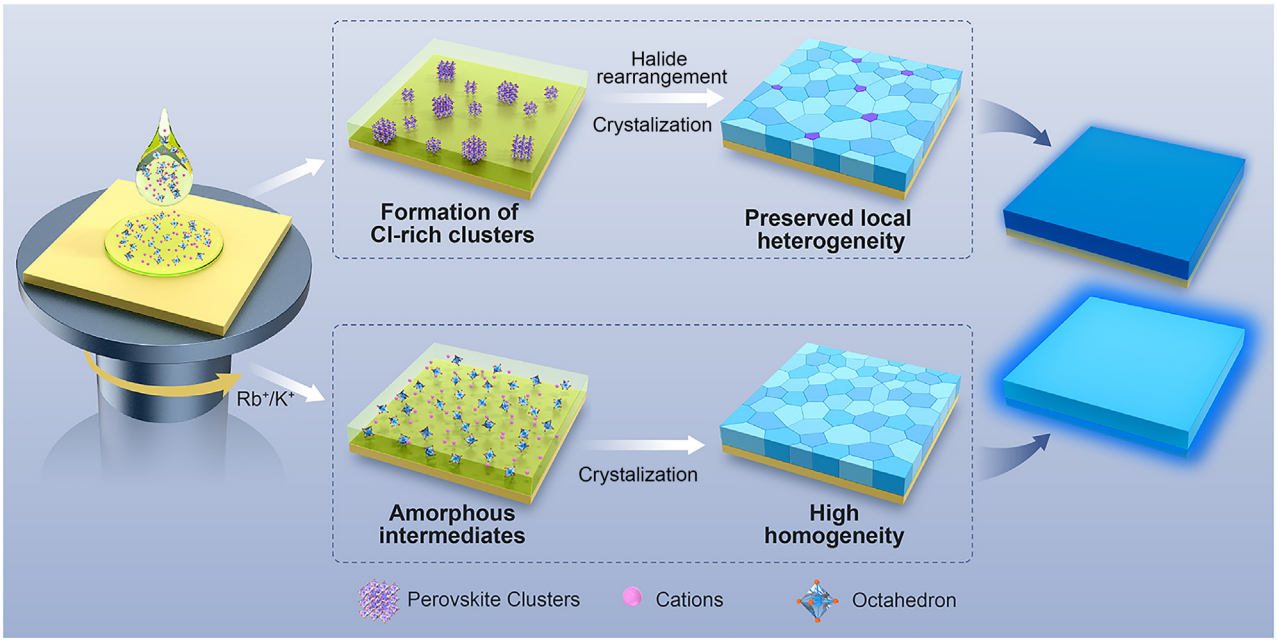

Figure 5. Schematic illustration highlighting the impact of the crystallization process on the local compositional heterogeneity of perovskites and the corresponding thin-film quality

The dash squares depict the crystallization process in control and target samples (i.e., with Rb/K addition). The upper panel suggests a fast nucleation of Cl-rich perovskite clusters, which are partially retained in perovskite films even after the halide-rearrangement process facilitated by vapor-assisted crystallization. The lower panel demonstrates a different scenario, where the intermediate phases undergo a direct conversion to perovskites with high homogeneity. The differences in the crystallization processes between the two scenarios ultimately lead to variations in the luminance properties of the thin films.

investigations on homogenizing local chemical compositions are highly demanded for developing more efficient blue PeLEDs.

EXPERIMENTAL PROCEDURES

Resource availability

Lead contact

Further information and requests for resources should be directed to and will be fulfilled by the lead contact, Feng Gao (feng.gao@liu.se).

Materials availability

This study did not generate new unique materials.

Data and code availability

All data are available upon reasonable request.

Materials

Lead bromide ($PbBr_2$; 99.999%), lead chloride ($PbCl_2$; 99.999%), PVP (average Mw ~55000), PVK (average Mn 25,000–50,000), and all the solvents were purchased from Sigma-Aldrich. Cesium bromide (CsBr, 99.999%) and rubidium bromide (RbBr, 99.8%) were purchased from Alfa-Aesar. 3,6,9,12,15-Pentaoxaheptadecane-1,17-diyl-bis-amine (NH_2-PEG_5-NH_2) was obtained from Bidepharm. Formamidinium bromide (FABr) was purchased from Greatcell Solar. TPBi was purchased from Xi'an Yuri Solar Co., Ltd. Aluminum, gold, and tungsten wire baskets were purchased from ZhongNuo Advanced Material (Beijing) Technology Co., Ltd.

Preparation of the perovskite solution

The perovskite precursor solution was prepared by mixing the precursor components with a stoichiometry of Cs^{+}:$(FA_{0.3-x}/Rb_x)^{+}$:Pb^{2+}:$[Br_{0.6}/Cl_{0.4}]^{-}$ = 1.2:0.3:1:3.5, where x = 0.1 or 0 in dimethyl sulfoxide (DMSO). The precursor concentration is 0.15 M as determined by Pb^{2+} in the precursors. The ratio of Rb^{+} in the precursor has been carefully optimized (Figure S26). The solution was stirred at 90°C overnight before use.

Device fabrication

ITO-coated glass substrates were sequentially cleaned with detergent and TL-1 (a mixture of water, 25% ammonia, and 28% hydrogen peroxide, 5:1:1 by volume). The ITO substrates were then treated with ultraviolet ozone cleaner for 20 min. Then NiO_x layers were deposited on the substrates at the speed of 3000 rpm for 30 s, followed by annealing at 130°C for 20 min in the air. Afterward, the NiO_x-coated substrates were transferred to the nitrogen-filled glove box. The PVK layer (dissolved in chlorobenzene, 4 mg mL^{-1}) was spin-coated at 3,000 rpm for 30 s, followed by annealing at 150°C for 30 min. To improve the surface wetting, a thin layer of PVP (dissolved in isopropyl alcohol, 2.5 mg mL^{-1}) was spun on the top of the PVK at 3,000 rpm for 30 s and annealed at 90°C for 10 min. After cooling to room temperature, the perovskite films were prepared using a previously reported vapor-assisted crystallization technique.[12] In brief, after spin coating (3000 rpm for 30 s), the wet precursor films were directly transferred into a Petri dish with 20 μL DMF. After 20 min of vapor treatment, the perovskite films were annealed at 70°C for 8 min. Next, the electron transport layer TPBi and LiF were deposited by using thermal evaporation under a base pressure of $\sim 10^{-7}$ torr. Finally, the 100 nm Al metal electrode was deposited through shadow masks. The active area of our devices is 7.25 mm^2, defined by the overlapping area of the top Al contacts with the ITO bottom electrode.

Device characterization

The characteristics of the current density-voltage-luminance and EL spectra without encapsulation, in a nitrogen-filled glovebox at room temperature. A Keithley 2400 digital source meter and integration sphere (FOIS-Ocean Optics) coupled with a QE Pro spectrometer (Ocean Optics) were used for the EL measurements, controlled by a homemade LabVIEW program. The absolute spectral radiant flux was calibrated using a standard Vis-NIR light source (HL-3P-INT-CAL plus; Ocean Optics). All the devices were tested on top of the integration sphere, where only forward light emission could be collected. The devices were swept from zero bias to forward bias with a step voltage of 0.05 V, lasting for 50 ms at each voltage step for stabilization. The operational lifetime of devices and spectral stability were measured using the same test system.

Perovskite film characterization

All the perovskite samples were deposited on ITO/NiO_x/PVK/PVP substrates under identical conditions as for the PeLEDs unless otherwise stated. Top-view scanning electron microscopy (SEM) images were tested by using Zeiss Gemini. Steady-state PL spectra of the perovskite films were recorded by a fluorescent spectrophotometer FL-7000, HITACHI with a 200 W Xe lamp as an excitation source. UV-vis absorbance spectra were collected using a PerkinElmer model Lambda 900. XRD patterns were measured by using a Bruker D8 Advance with the working voltage of 40 kV and current of 40 mA, step length of 0.02°, scanning speed of 0.1 s/step, scanning range: 10°–50° with an X-ray tube (Cu K_α, λ = 1.5406 Å).

In situ PL and transmittance measurements were performed by a homemade system using QE Pro as the spectrometer. For *in situ* PL tests, a 365 nm UV lamp as the excitation source. *In situ* transmittance tests were performed by using a solar simulator (AM 1.5G). An ND filter was used to decrease the light intensity to balance the SNR. The system configuration is depicted in Figure S27. The fluence-dependent PLQE were measured with a setup consisting of a 405 nm CW laser, integrating sphere (Edinburgh Instruments), and spectrometer (Andor; Oxford Instruments). All PL data were recalibrated by a standard lamp (HL-3-P-CAL; Ocean Optics).

Time-correlated single electron counting (TCSPC) measurements were measured using an Edinburgh Instruments FLS1000 with a 405 nm pulsed picosecond laser (EPL-405). We used a three-index fit exponential equation to model and fit the PL decay curves with the following formula, providing a mathematical means to extract the average lifetime:

$$A(t) = A_1 \exp\left(-\frac{\tau}{\tau_1}\right) + A_2 \exp\left(-\frac{\tau}{\tau_2}\right) + A_3 \exp\left(-\frac{\tau}{\tau_3}\right). \quad \text{(Equation 1)}$$

TEM of precursor films was performed using a TECNAI G2 F20 transmission electron microscope with an accelerating voltage of 200 kV and a Gatan SC200 charge-coupled device (CCD) camera.

STEM and EDX

The cross-sectional samples for STEM tests were made by an FEI-Focused Ion Beam (FIB) system (Helios Nanolab 600i). The high-angle angular dark field (HAADF) images were obtained by an FEI Titan-G2 Cs-corrected TEM with an accelerating voltage of 300 kV. The EDX mapping images were collected by four silicon drift windowless detectors (Super-EDX) in the microscope with an energy resolution of 137 eV.

Hyperspectral microscopy characterization

Hyperspectral images were captured using an IMA-VIS system developed by Photon etc. All the samples were measured using a 20× Nikon air objective and a 405 nm continuous-wave (CW) laser with an excitation intensity of 1 W cm^{-2}. All the samples were encapsulated with glass slides and UV-curable glue to avoid the influence of oxygen and humidity. The deposition process of all the samples used was consistent with the device manufacturing process. Multispectral image slices were obtained by scanning the angle of the grating relative to the emitted light from the sample, and the resulting three-dimensional data were stored in a hierarchical data format (HDF5). The spectral resolution is guided by the bandwidth of the holographic grating in the setup and is around 0.2 nm. For all the perovskite sample measurements, one second's integration time per wavelength slice and a step size of 2 nm across the wavelength were used.

The emitted light from all the samples was incident on a volume Bragg grating, which splits the light spectrally onto a CCD. The detector was a 1,040 × 1,392 resolution silicon CCD camera kept at 0°C by a thermoelectric cooler with an operational wavelength range of 400–1,000 nm.

TA spectroscopy

TA measurements were performed using a Helios setup. The transient dynamics in fs-ns time region (50 fs - 7 ns) was acquired by Helios that works in a nondegenerate pump-probe configuration. The pump pulses were generated from an optical parametric amplifier (OPerA Solo) that was pumped by a 1 kHz regenerative amplifier

(Coherent Libra, 800 nm, 50 fs). The samples are excited either with a 350 or 400 nm lasing pump source. A mode lock Ti-sapphire oscillator (Coherent Vitesse, 100 fs, 80 MHz) was used to seed the amplifier. The probe pulses were a white light continuum generated by passing the 800 nm femtosecond pulses through a 2 mm CaF_2 plate for UV part (250–650 nm).

GIWAXS

The GIWAXS measurements were performed in the Shanghai Synchrotron Radiation Facility (SSRF). The diffraction patterns were collected by a two-dimensional Rayonix MX225 detector with a distance of 293.3 mm between the perovskite samples and the detector. The wavelength of the X-ray was 1.24 Å (10 keV). All the samples were protected with nitrogen during the measurements. To accurately capture the detailed changes during the crystallization process of the sample, an exposure time of 10 s was adopted with an incidence angle of 0.2°. To avoid the interference of the Petri dish on the X-ray scattering signal during the *in situ* measurement, all samples were placed in a self-made setup using a cropped Petri dish with a polyurethane tape to simulate the actual sample solvent annealing process, where 20 μL of dimethylformamide (DMF) was dropped at the beginning of the measurement.

Impedance spectroscopy

All the devices were measured using a setup consisting of the Zurich Instruments MFLI lock-in amplifier with MF-IA and MF-MD options, a cryoprobe station Janis ST500 with a Lakeshore 336 temperature controller. The impedance spectroscopy measurements were carried out in the temperature range from 350 K to 225 K with 5 K steps, using liquid nitrogen for cooling. The capacitance in a C||R equivalence model was measured by applying an AC voltage with an amplitude of V_{ac} = 20 mV and varying the frequency from 3.1 Hz to 3.2 MHz. More details for theoretical models are summarized in Note S4.

Nanobeam X-ray fluorescence characterization

The elemental distribution of the perovskite film was investigated using synchrotron-based nanoprobe X-ray fluorescence at the NanoMAX beamline, at the MAX IV Laboratory in Lund, Sweden. The beam has a spot size of about 60 × 60 nm (vertical × horizontal), focused using a set of KB mirrors. The beam energy was fixed at 16.0 keV with an incident flux of 9.2 × 10^8 photons/s during the experiment. The step size for the measurement was 60 nm and the exposure time was about 50 ms per point. All the samples were deposited the same as the substrate of PeLEDs except that to deduct the noise signal of ITO glass. In this case, polished silicon wafers were used instead. All the samples were kept in a sealed container with nitrogen filled before measurement and accompanied by the nitrogen flow during the measurement. The n-XRF measurement was conducted with the backside Al contact facing the incident X-ray beam, with a full fluorescence spectrum collected point-by-point during mapping. All the measurements were performed in transmission geometry, with the sample facing the incident X-ray beam. A RaySpec single-element silicon drift detector (SDD), coupled with an XSPRESS3 pulse processor, was used to collect the X-ray fluorescence spectra, and PyMCA software was used to fit the data. The details for data interpretation and process are summarized in Note S3.

Before starting the formal measurement, we balanced the beam damage and the clarity of the data by adjusting the exposure time and incident flux. To avoid the test results being affected by the beam damage, we appropriately reduced the incident flux below the safe value to ensure that there is no obvious beam

damage before and after the measurement. From the above, we assert that the beam damage does not influence the conclusions from the analysis on our XRF maps.

SUPPLEMENTAL INFORMATION

Supplemental information can be found online at https://doi.org/10.1016/j.matt.2023.12.019.

ACKNOWLEDGMENTS

This work was supported by the National Natural Science Foundation of China (grants 52250060, 62288102, 62274135, 51903137, and 61890942), and Foshan Xianhu Laboratory of the Advanced Energy Science and Technology Guangdong Laboratory (grant XHT2020-005). The authors would like to thank the NanoMAX beamline at MAX IV in Lund, Sweden (proposal 20211260) and Shanghai Synchrotron Radiation Facility (SSRF) for providing the beamtime for measurement. C.D. and S.T. thank the DFG (Deutsche Forschungsgemeinschaft) for generous support within the framework of SPP 2196 project (PERFECT PVs). The research was funded by the European Research Council (ERC) under the European Union's Horizon 2020 research and innovation program (grant agreement 801847). L.A.B.M., Zhaojun Zhang, and J.W. also acknowledge funding support from the Olle Engkvist Foundation and Nano Lund and the students of the modern X-ray physics course for assistance with the measurements. Research conducted at MAX IV, a Swedish national user facility, is supported by the Swedish Research Council (contract 2018-07152), the Swedish Governmental Agency for Innovation Systems (contract 2018-04969), and Formas (contract 2019-02496). K.J. and S.D.S. acknowledge funding from the Royal Society, the Engineering and Physical Sciences Research Council (EPSRC; grants EP/R023980/1, EP/V06164X/1, and EP/V027131/1), and the European Research Council under the European Union's Horizon 2020 research and innovation program (HYPERION; grant agreement 756962). S.D.S. acknowledges funding from the Royal Society and Tata Group (grant UF150033). The work at Linköping was financially supported by the Swedish Energy Agency Energimyndigheten (grants P2019-48758 and P2022-00394) and the Swedish Government Strategic Research Area in Materials Science on Functional Materials at Linköping University (faculty grant SFO-Mat-LiU 2009-00971). X.L. acknowledges financial support from the China Scholarship Council (grant 202006210284) and the Tsinghua Scholarship for short-term overseas graduate studies.

AUTHOR CONTRIBUTIONS

W.X. and F.G. conceived and supervised the project. X.L. and W.X. carried out most of the experiments and analyzed the data. K.J. and S.K. performed hyperspectral microscopy characterization and analyzed the data under the supervision of S.D.S. L.A.B.M., H.C., and Zhaojun Zhang performed XRF and analyzed the data under the supervision of J.W. W.Q. performed TA measurements and analyzed the data under the supervision of M.L. S.T. performed admittance spectroscopy and analyzed the data under the supervision of C.D. G.Z. performed *in situ* GIWAXS measurements and analyzed the data. C.Y. built the fluence-dependent PLQY setup and contributed to analysis of the data. Zeyu Zhang and Y.L. performed STEM-EDX measurements. H.Z. analyzed the TEM results. L.D., D.Z., and W.X. supervised X.L. X.L., W.X., and F.G. wrote the manuscript. S.D.S., Y.Z., M.K., D.M., and W. H. contributed to data analysis and provided revisions to the manuscript. All authors discussed the results and commented on the manuscript.

DECLARATION OF INTERESTS

The authors declare no competing interests.

Received: July 26, 2023
Revised: October 1, 2023
Accepted: December 12, 2023
Published: January 12, 2024

REFERENCES

1. Li, W., Wang, Z., Deschler, F., Gao, S., Friend, R.H., and Cheetham, A.K. (2017). Chemically diverse and multifunctional hybrid organic–inorganic perovskites. Nat. Rev. Mater. *2*, 16099–18.

2. Luo, Y., Aharon, S., Stuckelberger, M., Magaña, E., Lai, B., Bertoni, M.I., Etgar, L., and Fenning, D.P. (2018). The relationship between chemical flexibility and nanoscale charge collection in hybrid halide perovskites. Adv. Funct. Mater. *28*, 1706995.

3. Brandt, R.E., Poindexter, J.R., Gorai, P., Kurchin, R.C., Hoye, R.L.Z., Nienhaus, L., Wilson, M.W.B., Polizzotti, J.A., Sereika, R., Žaltauskas, R., et al. (2017). Searching for "defect-tolerant" photovoltaic materials: Combined theoretical and experimental screening. Chem. Mater. *29*, 4667–4674.

4. Frohna, K., Anaya, M., Macpherson, S., Sung, J., Doherty, T.A.S., Chiang, Y.H., Winchester, A.J., Orr, K.W.P., Parker, J.E., Quinn, P.D., et al. (2022). Nanoscale chemical heterogeneity dominates the optoelectronic response of alloyed perovskite solar cells. Nat. Nanotechnol. *17*, 190–196.

5. Kim, G.W., and Petrozza, A. (2020). Defect tolerance and intolerance in metal-halide perovskites. Adv. Energy Mater. *10*.

6. Erodici, M.P., Pierone, P.J., Hartono, N.T.P., Hidalgo, J., Lai, B., Buonassisi, T., Correa-Baena, J.-P., and Sher, M.-J. (2021). Enhanced charge carrier lifetime and mobility as a result of Rb and Cs incorporation in hybrid perovskite. Appl. Phys. Lett. *118*.

7. Gratia, P., Grancini, G., Audinot, J.N., Jeanbourquin, X., Mosconi, E., Zimmermann, I., Dowsett, D., Lee, Y., Grätzel, M., De Angelis, F., et al. (2016). Intrinsic halide segregation at nanometer scale determines the high efficiency of mixed cation/mixed halide perovskite solar cells. J. Am. Chem. Soc. *138*, 15821–15824.

8. Xi, J., Byeon, J., Kim, U., Bang, K., Han, G.R., Kim, J.-Y., Yoon, J., Dong, H., Wu, Z., Divitini, G., et al. (2021). Abnormal spatial heterogeneity governing the charge-carrier mechanism in efficient Ruddlesden–Popper perovskite solar cells. Energy Environ. Sci. *14*, 4915–4925.

9. Vashishtha, P., Ng, M., Shivarudraiah, S.B., and Halpert, J.E. (2018). High efficiency blue and green light-emitting diodes using Ruddlesden–Popper inorganic mixed halide perovskites with butylammonium interlayers. Chem. Mater. *31*, 83–89.

10. Cheng, L., Yi, C., Tong, Y., Zhu, L., Kusch, G., Wang, X., Wang, X., Jiang, T., Zhang, H., Zhang, J., et al. (2020). Halide homogenization for high-performance blue perovskite electroluminescence. Research *2020*, 9017871.

11. Du, P., Li, J., Wang, L., Liu, J., Li, S., Liu, N., Li, Y., Zhang, M., Gao, L., Ma, Y., and Tang, J. (2019). Vacuum-deposited blue inorganic perovskite light-emitting diodes. ACS Appl. Mater. Interfaces *11*, 47083–47090.

12. Karlsson, M., Yi, Z., Reichert, S., Luo, X., Lin, W., Zhang, Z., Bao, C., Zhang, R., Bai, S., Zheng, G., et al. (2021). Mixed halide perovskites for spectrally stable and high-efficiency blue light-emitting diodes. Nat. Commun. *12*, 361.

13. Wang, Q., Wang, X., Yang, Z., Zhou, N., Deng, Y., Zhao, J., Xiao, X., Rudd, P., Moran, A., Yan, Y., and Huang, J. (2019). Efficient sky-blue perovskite light-emitting diodes via photoluminescence enhancement. Nat. Commun. *10*, 5633.

14. Ma, D., Todorović, P., Meshkat, S., Saidaminov, M.I., Wang, Y.K., Chen, B., Li, P., Scheffel, B., Quintero-Bermudez, R., Fan, J.Z., et al. (2020). Chloride insertion-immobilization enables bright, narrowband, and stable blue-emitting perovskite diodes. J. Am. Chem. Soc. *142*, 5126–5134.

15. Nenon, D.P., Pressler, K., Kang, J., Koscher, B.A., Olshansky, J.H., Osowiecki, W.T., Koc, M.A., Wang, L.W., and Alivisatos, A.P. (2018). Design principles for trap-free $CsPbX_3$ nanocrystals: Enumerating and eliminating surface halide vacancies with softer Lewis Bases. J. Am. Chem. Soc. *140*, 17760–17772.

16. Zheng, X., Yuan, S., Liu, J., Yin, J., Yuan, F., Shen, W.-S., Yao, K., Wei, M., Zhou, C., Song, K., et al. (2020). Chlorine vacancy passivation in mixed halide perovskite quantum dots by organic pseudohalides enables efficient Rec. 2020 blue light-emitting diodes. ACS Energy Lett. *5*, 793–798.

17. Li, Z., Chen, Z., Yang, Y., Xue, Q., Yip, H.L., and Cao, Y. (2019). Modulation of recombination zone position for quasi-two-dimensional blue perovskite light-emitting diodes with efficiency exceeding 5. Nat. Commun. *10*, 1027.

18. Ho, H.P., Harrison, I., Baba-Ali, N., and Tuck, B. (1991). Diffusion-induced defects in GaAs by zinc and the effects of post-diffusion anneal. J. Appl. Phys. *69*, 3494–3502.

19. Zou, Y., Teng, P., Xu, W., Zheng, G., Lin, W., Yin, J., Kobera, L., Abbrent, S., Li, X., Steele, J.A., et al. (2021). Manipulating crystallization dynamics through chelating molecules for bright perovskite emitters. Nat. Commun. *12*, 4831.

20. Xu, W., Hu, Q., Bai, S., Bao, C., Miao, Y., Yuan, Z., Borzda, T., Barker, A.J., Tyukalova, E., Hu, Z., et al. (2019). Rational molecular passivation for high-performance perovskite light-emitting diodes. Nat. Photon. *13*, 418–424.

21. Zhang, L., Yang, X., Jiang, Q., Wang, P., Yin, Z., Zhang, X., Tan, H., Yang, Y.M., Wei, M., Sutherland, B.R., et al. (2017). Ultra-bright and highly efficient inorganic based perovskite light-emitting diodes. Nat. Commun. *8*, 15640.

22. Wu, K., Bera, A., Ma, C., Du, Y., Yang, Y., Li, L., and Wu, T. (2014). Temperature-dependent excitonic photoluminescence of hybrid organometal halide perovskite films. Phys. Chem. Chem. Phys. *16*, 22476–22481.

23. Schmidt, T., Lischka, K., and Zulehner, W. (1992). Excitation-power dependence of the near-band-edge photoluminescence of semiconductors. Phys. Rev. B *45*, 8989–8994.

24. Vanecek, M., and Poruba, A. (2002). Fourier-transform photocurrent spectroscopy of microcrystalline silicon for solar cells. Appl. Phys. Lett. *80*, 719–721.

25. Zhang, W., Pathak, S., Sakai, N., Stergiopoulos, T., Nayak, P.K., Noel, N.K., Haghighirad, A.A., Burlakov, V.M., DeQuilettes, D.W., Sadhanala, A., et al. (2015). Enhanced optoelectronic quality of perovskite thin films with hypophosphorous acid for planar heterojunction solar cells. Nat. Commun. *6*. 10030–9.

26. Subedi, B., Li, C., Chen, C., Liu, D., Junda, M.M., Song, Z., Yan, Y., and Podraza, N.J. (2022). Urbach energy and open-circuit voltage deficit for mixed anion–cation perovskite solar cells. ACS Appl. Mater. Interfaces *14*, 7796–7804.

27. Teng, P., Reichert, S., Xu, W., Yang, S.-C., Fu, F., Zou, Y., Yin, C., Bao, C., Karlsson, M., and Liu, X. (2021). Degradation and self-repairing in perovskite light-emitting diodes. Matter *4*, 3710–3724.

28. Tammireddy, S., Reichert, S., An, Q., Taylor, A.D., Ji, R., Paulus, F., Vaynzof, Y., and Deibel, C. (2021). Temperature-dependent ionic conductivity and properties of iodine-related defects in metal halide perovskites. ACS Energy Lett. *7*, 310–319.

29. Reichert, S., Flemming, J., An, Q., Vaynzof, Y., Pietschmann, J.-F., and Deibel, C. (2020). Ionic-defect distribution revealed by improved evaluation of deep-level transient spectroscopy on perovskite solar cells. Phys. Rev. Applied *13*.

30. Barker, A.J., Sadhanala, A., Deschler, F., Gandini, M., Senanayak, S.P., Pearce, P.M.,

Mosconi, E., Pearson, A.J., Wu, Y., Srimath Kandada, A.R., et al. (2017). Defect-assisted photoinduced halide segregation in mixed-halide perovskite thin films. ACS Energy Lett. *2*, 1416–1424.

31. Abdi-Jalebi, M., Andaji-Garmaroudi, Z., Cacovich, S., Stavrakas, C., Philippe, B., Richter, J.M., Alsari, M., Booker, E.P., Hutter, E.M., Pearson, A.J., et al. (2018). Maximizing and stabilizing luminescence from halide perovskites with potassium passivation. Nature *555*, 497–501.

32. Doherty, T.A.S., Winchester, A.J., Macpherson, S., Johnstone, D.N., Pareek, V., Tennyson, E.M., Kosar, S., Kosasih, F.U., Anaya, M., Abdi-Jalebi, M., et al. (2020). Performance-limiting nanoscale trap clusters at grain junctions in halide perovskites. Nature *580*, 360–366.

33. Macpherson, S., Doherty, T.A.S., Winchester, A.J., Kosar, S., Johnstone, D.N., Chiang, Y.H., Galkowski, K., Anaya, M., Frohna, K., Iqbal, A.N., et al. (2022). Local nanoscale phase impurities are degradation sites in halide perovskites. Nature *607*, 294–300.

34. Tennyson, E.M., Doherty, T.A.S., and Stranks, S.D. (2019). Heterogeneity at multiple length scales in halide perovskite semiconductors. Nat. Rev. Mater. *4*, 573–587.

35. Correa-Baena, J.-P., Luo, Y., Brenner, T.M., Snaider, J., Sun, S., Li, X., Jensen, M.A., Hartono, N.T.P., Nienhaus, L., Wieghold, S., et al. (2019). Homogenized halides and alkali cation segregation in alloyed organic-inorganic perovskites. Science *363*, 627–631.

36. Schöppe, P., Schönherr, S., Jackson, P., Wuerz, R., Wisniewski, W., Ritzer, M., Zapf, M., Johannes, A., Schnohr, C.S., and Ronning, C. (2018). Overall distribution of rubidium in highly efficient Cu(In,Ga)Se_2 solar cells. ACS Appl. Mater. Interfaces *10*, 40592–40598.

37. Queisser, H.J., and Haller, E.E. (1998). Defects in semiconductors: Some fatal, some vital. Science *281*, 945–950.

38. Huang, T., Tan, S., Nuryyeva, S., Yavuz, I., Babbe, F., Zhao, Y., Abdelsamie, M., Weber, M.H., Wang, R., Houk, K.N., et al. (2021). Performance-limiting formation dynamics in mixed-halide perovskites. Sci. Adv. *7*, eabj1799.

39. Knight, A.J., Borchert, J., Oliver, R.D.J., Patel, J.B., Radaelli, P.G., Snaith, H.J., Johnston, M.B., and Herz, L.M. (2021). Halide segregation in mixed-halide perovskites: Influence of A-site cations. ACS Energy Lett. *6*, 799–808.

40. Ahmed, G.H., El-Demellawi, J.K., Yin, J., Pan, J., Velusamy, D.B., Hedhili, M.N., Alarousu, E., Bakr, O.M., Alshareef, H.N., and Mohammed, O.F. (2018). Giant photoluminescence enhancement in $CsPbCl_3$ perovskite nanocrystals by simultaneous dual-surface passivation. ACS Energy Lett. *3*, 2301–2307.

41. Chen, Y., Liu, Y., and Hong, M. (2020). Cation-doping matters in caesium lead halide perovskite nanocrystals: From physicochemical fundamentals to optoelectronic applications. Nanoscale *12*, 12228–12248.

42. Kubicki, D.J., Prochowicz, D., Hofstetter, A., Zakeeruddin, S.M., Grätzel, M., and Emsley, L. (2017). Phase segregation in Cs-Rb- and K-doped mixed-cation $(MA)_x(FA)_{1-x}PbI_3$ hybrid perovskites from solid-state NMR. J. Am. Chem. Soc. *139*, 14173–14180.

43. Saliba, M., Matsui, T., Domanski, K., Seo, J.Y., Ummadisingu, A., Zakeeruddin, S.M., Correa-Baena, J.P., Tress, W.R., Abate, A., Hagfeldt, A., and Grätzel, M. (2016). Incorporation of rubidium cations into perovskite solar cells improves photovoltaic performance. Science *354*, 206–209.